Arabian Journal of Chemistry (2022) **15**, 104230

King Saud University

Arabian Journal of Chemistry

www.ksu.edu.sa
www.sciencedirect.com

ORIGINAL ARTICLE

One-pot synthesis, X-ray crystal structure, and identification of potential molecules against COVID-19 main protease through structure-guided modeling and simulation approach

Youness El Bakri [a,*], **Malahat Musrat Kurbanova** [b], **Sabir Ali Siddique** [c], **Sajjad Ahmad** [d], **Souraya Goumri-Said** [e,**]

[a] *Department of Theoretical and Applied Chemistry, South Ural State University, Lenin prospect 76, Chelyabinsk 454080, Russian Federation*
[b] *Baku State University, Organic Chemistry Department, Z. Khalilov 23, Baku, AZ 1148, Azerbaijan*
[c] *Center for Organic Chemistry, School of Chemistry, University of the Punjab, Lahore 54590, Pakistan*
[d] *Department of Health and Biological Sciences, Abasyn University, Peshawar 25000, Pakistan*
[e] *College of Science, Physics department, Alfaisal University, Riyadh 11533, Saudi Arabia*

Received 2 March 2022; accepted 31 August 2022
Available online 15 September 2022

KEYWORDS

Dihydropyrimidinones;
SARS-CoV-2 M^{pro};
Hirshfeld surface analysis;
NBO analysis;
Molecular docking

Abstract Although antimicrobial resistance before the Covid-19 pandemic is a top priority for global public health, research is already ongoing on novel organic compounds with antimicrobial and antiviral properties in changing medical environments in connection with Covid 19. Thanks to the Biginelli reaction, which allows the synthesis of pyrimidine compounds, blockers of calcium channels, antibodies, antiviral, antimicrobial, anti-inflammatory, or antioxidant therapeutic compounds were investigated. In this paper, we aim to present Biginelli's synthesis, its therapeutic properties, and the structural–functional relationship in the test compounds that allows the synthesis of antimicrobial compounds. Both the DFT and TD-DFT computations of spectral data, molecular orbitals (HOMO, LUMO) analysis, and electrostatic potential (MEP) surfaces are carried out as an add-on to synthetic research. Hirshfeld surface analysis was also used to segregate the different intermolecular hydrogen bonds involved in the molecular packing strength. Natural Bond Orbital (NBO) investigation endorses the existence of intermolecular interactions mediated by lone pair, bonding, and anti-bonding orbitals. The dipole moment, linear polarizability, and first hyperpolarizabilities

** Corresponding author.
* Corresponding author.
E-mail addresses: yns.elbakri@gmail.com (Y. El Bakri), sosaid@alfaisal.edu (S. Goumri-Said).
Peer review under responsibility of King Saud University.

Production and hosting by Elsevier

https://doi.org/10.1016/j.arabjc.2022.104230

have been explored as molecular parameters. All findings based on DFT exhibit the best consistency with experimental findings, implying that synthesized molecules are highly stable. To better understand the binding mechanism of the SARS-CoV-2 M^{pro}, we performed molecular docking, molecular dynamics (MD) simulations, and binding free energy calculations.

1. Introduction

In 1843, Pietro Biginelli was discovered. The reaction is based on the condensation of aldehydes, urea, and 1,3-dicarbonyl compounds in an acidic medium. As a result of the synthesis, heterocyclic systems of dihydropyrimidinones are formed, which play an important role in the construction of biomolecules such as DNA and RNA. In addition, in the fields of application, the synthesis and development of materials with optical properties, the design of polymers, dyes, and adhesives are also included. The most widely used area of biological impact is medicine. The multicomponent nature of the Biginelli reaction provides large product diversity bearing different pharmacophoric groups in the structure of dihydropyrimidines, which ensure optimal supramolecular interactions with a specific biological target (molecular recognition) and triggers or blocks its biological response. Investigations through molecular manipulations reveal that this class of compounds demonstrate antiviral, anti-filarial, antifungal, analgesic, anti-leishmanial, antiproliferative, antitumor, anti-convulsant, antibacterial, anti-inflammatory, anti-hypertensive, melanin-concentrating hormone 1 receptor antagonist, anti-HIV, antiepileptic, antidiabetic, anti-SARS, anti-malarial, pages-1 inhibitors, anti-hyperglycemic, antitubercular, TRPA1 antagonist, miscellaneous, potassium and calcium channels, and a1a adrenergic antagonists. Similarly, the structural core of quinoline is frequently associated with medicinal applications such as anticancer, antimicrobial, HIV-1 integrase inhibition, HIV protease inhibitors, antileishmanial activity, NK-3 receptor antagonists, PLT antagonists, and antimalarial activity. As a result of these studies, the use of various types of drugs such as riboflavin, idoxuridine, aminophylline, emivirine, 5-fluorouracil, methylthiouracil, batzelladine A, and B based on dihydropyrimidines has allowed widespread use in medicine. Due to the utmost importance of dihydropyrimidines in pharmaceutics, robust, efficient, cost-effective, and "green" chemical synthesis and transformations of dihydropyrimidine scaffolds were developed (Kaur et al., 2015; Nagarajaiah et al., 2016; Terracciano et al., 2015; Yadlapalli et al., 2012; Zhu et al., 2010).(See Scheme 1 Scheme 2.).

In the biological aspects of the motif, fixed molecules are needed that can easily be obtained for evaluation/study, and in 1930, the woolly-containing activity of these molecules was patented. These molecules bore similarities to the clinical spectrum of nifedipine. Biginelli researched by analogy with their analogs, and later it turned out that they showed the similarity of natural sea alkaloids with batzelladine B. All three building blocks are aldehyde, active methylene, and urea and are caused by the molecular diversity of dihydropyrimidines, which have a multicomponent reaction. The potent pyrimidine molecules produced by the Bignelli reaction have been successfully used and experimented with in stress and pollution-induced diseases. The following are selective molecules having significant activity, and they are examined with clinically used drugs *in vivo*/*in vitro,* establishing QSAR (Ashok et al., 2007; Chiang et al., 2009; Chitra et al., 2010; Deshmukh et al., 2009; Kidwai et al., 2005; Rajanarendar et al., 2010). There are several reasons that Biginelli's reaction has been studied in recent decades (Bais et al., 2020; de Fátima et al., 2015; Gireesh et al., 2013; Ismaili et al., 2008; Kaur et al., 2017; Li et al., 2020; Liu et al., 2019; Mokale et al., 2010; Rani et al., 2016; Sawant and Sarode, 2011; Silva et al., 2015).

As well as the inhibitory potential of antimicrobial and antibacterial pyrimidine derivatives has been evaluated against SARS-CoV-2 (Khan et al., 2021). Considering the importance of this class of compound, herein, two compounds are synthesized, characterized, and used in different computational approaches to unveil their anti-SARS-CoV-2 activity. Computational drug designing has been a good platform for predicting the binding capacity of compounds to different therapeutic targets and thus saves time and cost that are usually required in experimental testing. In this study, the docking studies are revalidated by more sophisticated molecular dynamics simulation

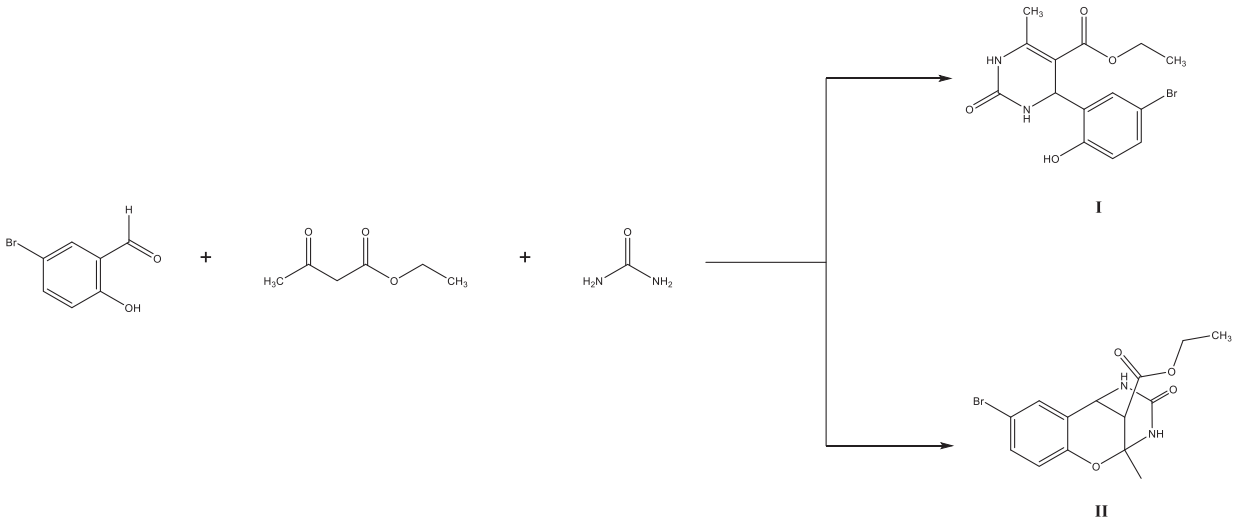

Scheme 1 Synthesis of compounds **(I)** and **(II)**.

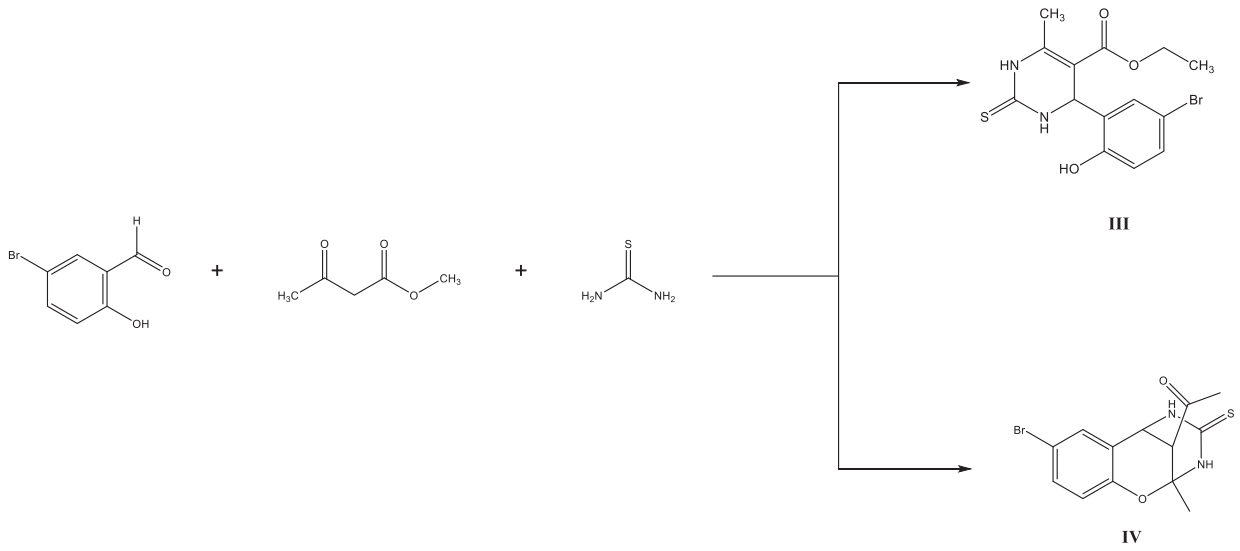

Scheme 2 Synthesis of compounds **(III)** and **(IV)**.

and binding free energy analysis. In a nutshell, the findings obtained in this study could be useful for experimentalists to test the compounds against SARS-CoV-2 and in particular to be tested in enzymatic assay against the SARS-CoV-2 main protease enzyme.

2. Materials and methods

2.1. Instrumentation

The NMR spectra were recorded at 25 °C from solutions in DMSO d_6 on a Bruker-300 spectrometer operating at 300 MHz. The IR spectra were obtained on a Specord 75IR instrument from samples dispersed in mineral oil. The progress of reactions and the purity of products were monitored by TLC.

2.2. X-ray diffraction study

Single crystals of compounds **I** and **IV** suitable for X-ray analysis were obtained by double recrystallization from ethanol (Kurbanova, 2010). The X-ray diffraction data were acquired on a Bruker APEX II CCD diffractometer (100 k), λMoK_α irradiation, graphite monochromator, φ- and ω-scanning, 20max = 56°). The structures were solved by the direct method and refined by the least-squares procedure in an anisotropic approximation for non-hydrogen atoms. Hydrogen atoms in the hydroxy and amino groups were localized by the Fourier difference syntheses, and their positions were refined in an isotropic approximation with fixed positional and thermal parameters. The positions of the other hydrogen atoms were calculated based on geometry considerations and were refined in isotropic approximation with fixed positional and thermal parameters. All calculations were performed using the SHELXTL PLUS and SADABS software packages (Sheldrick, 2003, n.d.). The complete sets of crystallographic data for compounds **I** and **IV** were deposited at the Cambridge Crystallographic Data Centre (entry nos. **CCDC 694,407** and **CCDC 707349**).

2.3. Computational studies

Computational studies of the compounds were performed to evaluate their binding affinity for different anti-SARS-CoV-2 targets. These targets include the SARS-CoV-2 main protease enzyme, RNA-dependent RNA polymerase (RdRp), and envelop (E) protein. The crystal structures of these targets were retrieved from protein data banks and underwent preprocessing in UCSF Chimera 1.15 (Pettersen et al., 2004). The PDB IDs used for retrieval of the proteins are the main protease enzyme (6y2e), RdRp (7D4F), and E (7M4R). During preprocessing, all co-crystalized ligands were removed, and the structures were relaxed using the steepest descent and conjugate gradient algorithms using default parameters.

2.4. Molecular docking and dynamics simulation studies

Molecular docking of the compounds with the targeted enzymes was conducted through AutoDock Vina software (Trott and Olson, 2010). Before that, the compound structure was drawn in ChemDraw 12.0 (Cousins, 2011) and processed into.pdb format. The proteins were also imported into the docking software. The grid box was set around the active site of the enzyme along a 15 Å on XYZ axis. The number of compounds docked was set at 100. Each compound conformation is associated with binding energy, and the one with the lowest score was complexed with the best-docked enzyme. Visualization of complexes was done in UCSF Chimera 1.15 (Kaliappan and Bombay, 2016) and Discovery studio v2021 (Biovia, 2017). Further, the best-docked complex for both compounds was subjected to molecular dynamics simulation for 300 ns. Simulations were performed via AMBER20 software (Case et al., 2020). In the simulation, the protein parameters were prepared using ff14SB (Maier et al., 2015), while the compounds were parameterized using GAFF (He et al., 2020). Energy minimization of complexes was accomplished via steepest descent and conjugate gradient steps, each of which was run for 1000 cycles. Heating was achieved at 310 K for 100 ps. Equilibration was done for 200 ps. SHAKE and

Langevin were used to constrain hydrogen bonds and maintain temperature during a production run, respectively (Izaguirre et al., 2001; Kräutler et al., 2001). CPPTRAJ was applied to analyze simulation trajectories (Roe and Cheatham III, 2013). MMPBSA.py module of AMBER was considered for MMGBSA and MMPBSA binding free energies estimation on 100 frames of simulation trajectories (Genheden and Ryde, 2015; Miller et al., 2012).

3. Results and discussion

3.1. Chemical synthesis

The Biginelli reaction of salicylaldehyde derivatives can lead to the formation of 2 types of dihydropyrimidines (Kurbanova, 2010). The reaction of 5-bromosalicylaldehyde with ethyl acetoacetate and urea in the presence of trichloroacetic acid gave, depending on the conditions, ethyl 4-(5-bromo-2-hydroxyphenyl)-6-methyl-2-oxo-1,2,3,4-tetrahydropyrimidine-5-carboxylate (**I**) or ethyl 8-bromo-2-methyl-4-oxo-3,4,5,6-tetrahydro-2*H*-2,6-methanobenzo[g][1,3,5]oxadiazocine-11-carboxylate **(II)**. Ester, **I** was formed when the reactants were heated for 2–4 h in boiling ethanol, whereas bicyclic compound II was isolated when the reaction mixture was heated for 7–9 h at 40 °C.

A mixture of 0.025 mol of 5-bromosalicylaldehyde, 0.038 mol of ethyl acetoacetate, 0.025 mol of urea, and 25 mg of trichloroacetic acid in 10 ml of ethanol was stirred for 2–4 h on heating under reflux. The progress of the reaction was monitored by TLC. When the reaction was complete, the mixture was cooled to room temperature, and the precipitate was filtered off, washed with ethanol, dried, and recrystallized from aqueous ethanol.

The structure of compound **I** was proved by IR and NMR spectroscopy and **X-ray** diffraction data.

Ethyl 4-(5-bromo-2-hydroxyphenyl)-6-methyl-2-oxo-1,2,3,4-tetrahydropyrimidine-5-carboxylate (I). Yield 75 %, mp = 190–191 °C. IR spectrum, v, cm^{-1}: 3325, 1745, 1660. ^1H NMR spectrum, v, ppm: 1.30 t (3H, CH_2CH_3), 2.57 s (3H, CH_3), 4.25 q (2H, CH_2O), 5.70 s (1H, CH), 7.70–7.00 m (4H, Harom), 8.00 s (1H, NH), 9.41 s (1H, NH), 10.11 s (1H, OH).(See Fig. 1).

Ethyl 8-bromo-2-methyl-4-oxo-3,4,5,6-tetrahydro-2*H*-2,6-methanobenzo[g][1,3,5]

oxadiazocine-11-carboxylate (II) Yield 55 %, mp = 197–199 °C. IR spectrum, v, cm^{-1}: 3350, 1740, 1680. ^1H NMR spectrum, v, ppm: 1.27 t (3H, CH_2CH_3), 2.35 s (3H, CH_3), 3.27 d (1H, CH), 4.16 q (2H, CH_2O), 4.46 d (1H, CH), 6.77–7.21 m (3H, H_{arom}), 8.36 s (1H, NH), 8.41 s (1H, NH).

X-ray crystallographic analysis was performed by double crystallization of compound **I** in ethyl alcohol (Kurbanova et al., 2009). The monoclinic, yellow crystals, with sizes 0.20 × 0.20 × 0.20 mm^3, one striped: a = 9.3207(2), b = 16.841 (2), c = 10.0908(13) Å, β = 116.678(1)°, V = 1415.3(3) $Å^3$, space group $P2_1/n$, Z = 4, ds = 1.667 q/sm^3, μ = 2.922 mm^{-1} were obtained.

For comparison, three-component condensation of 5-bromosalicylaldehyde with acetylacetone and thiourea was examined. Under analogous conditions, the products were l-[4-(5-bromo-2-hydroxyphenyl)-6-methyl-2-thioxo-1,2,3,4-tetrahydropyrimidin-5-yl]-ethanone (**Ill**) and 1-(8-bromo-2-methyl-4-thioxo-3,4,5,6-tetrahydro-2H-2,6-methanobenzo[g][1,3,5]oxadiazocin-11-yl)ethan-1-one **(IV)**.

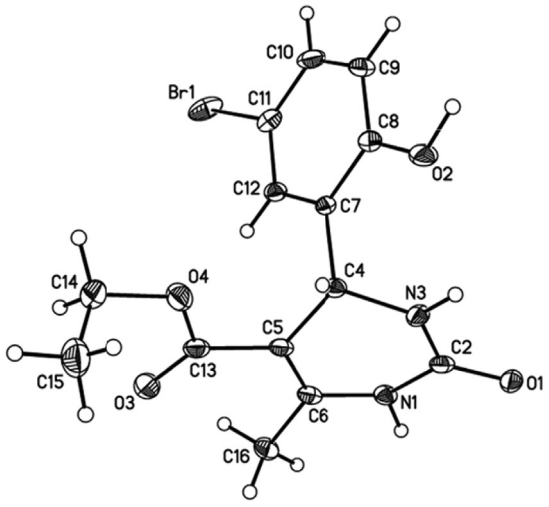

Fig. 1 Structure of **I** according to the X-ray diffraction data.

A mixture of 0.025 mol of 5-bromosalicylaldehyde, 0.038 mol of acetylacetone, 0.025 mol of thiourea, and 25 mg of trichloroacetic acid in 10 ml of ethanol was stirred for 2–4 h on heating under reflux. The progress of the reaction was monitored by TLC. When the reaction was completed, the mixture was cooled to room temperature, and the precipitate was filtered off, washed with ethanol, dried, and recrystallized from aqueous ethanol.

Compound **IV** was isolated as a crystalline substance and its structure was proved by IR and NMR spectroscopy and confirmed by X-ray analysis.

1-[4-(5-Bromo-2-hydroxypheny1)-6-methyl-2-thioxo-1,2,3,4-tetrahydropyrimidin-5-yl[ethanone (III).

Yield 75 %, mp = 175 °C. IR spectrum, v, cm^{-1}: 3345, 1665. ^1H NMR spectrum, o, ppm: 1.90 s (3H, CH_3), 2.47 s (3H, CH_3), 5.57 s (1H, CH), 7.10 s (1H, NH), 7.36–7.45 m (4H, H_{arom}), 8.14 s (1H, NH), 9.50 s (1H, OH).

1-(8-bromo-2-methyl-4-thioxo-3,4,5,6-tetrahydro-2H-2,6-methanobenzo[g][1,3,5]

3.2. oxadiazocin-11-yl)ethan-1-one (IV).

Yield 55 %, mp = 187–188 °C. IR spectrum, v, cm^{-1}: 3350, 1670. ^1H NMR spectrum, o, ppm: 1.79 s (3H, CH_3), 2.31 s (3H, CH_3), 3.33 d (I H, CH), 4.59 d (IH, CH), 6.84–7.20 m (3H, H_{arom}), 8.97 s (1H, NH), 9.12 s (1H, NH).

X-ray crystallographic analysis was performed by double crystallization of compound **IV** in ethyl alcohol. The monoclinic, yellow crystals, with sizes 0.20 × 0.20 × 0.30 mm^3, one striped: a = 16.845(3), b = 11.374(2), c = 14.680(3) Å, β = 103.822(2)°, V = 2731.2(9) Å, space group $C2/c$, Z = 8, d_c = 1.660 q/sm^3, μ = 3.162 mm^{-1} were obtained.

3.3. Hirshfeld surface analysis and 2D fingerprint plots

With the Hirshfeld surface, it is possible to witness intermolecular interactions and fashions in crystal packing (Maity et al.,

2018). The compounds **I** and **IV** were subjected to the Hirshfeld surface mapping across the normalized contact distance d_{norm} shown in Fig. 4. The color schemes shown in the map are red, blue, and white. The red (d_{norm} is negative) and blue (d_{norm} is positive) colored regions on the surface are from shorter and longer contacts than van der Waals radii respectively, whereas the white areas indicate the van der Waals radii of the contacts, or d_{norm} = 0 (McKinnon et al., 2007). In the brighter red zone, hydrogen bonding is responsible for the strong interactions, but electron density in the blue zone represents the weaker interactions. Qualitative measures of morphological structure, such as the "shape index," can be sensitive to even the tiniest changes in surface curvature (or curvedness). The concave region with red triangles in the shape index of atoms of a molecule represents the C—H···π and π···π stacking interactions, while convex regions with blue triangles represent aromatic ring atoms inside the surface. For compounds **I** and **IV**, massive green flat areas with blue outlines on the relatively curved surfaces were observed due to the π···π stacking interactions as shown in Fig. 3.

The intermolecular percent contribution of all kinds of contacts to the overall Hirshfeld surface area was calculated using 2D fingerprint plots (Seth, 2018). Fig. 4 shows the 2D fingerprint of all the contacts. The major contribution of both **I** and **IV** is from H—H contacts, 38.0 %, and 37.1 % respectively, to the total Hirshfeld surface area. The remaining contributions of C1 are from O—H, C—H, Br-H, Br-C, and N—H contacts, which contribute about 12.3 %, 9.6 %, 8.1 %, 2.1 %, 1.7 % respectively to the Hirshfeld surface area. The remaining contributions of *C*2 are from Br-H, O—H, H—S, C—H, C—C, Br-C, Br-Br, and Br-S contacts, which contribute about 8.6 %, 7.2 %, 5.6 %, 5.6 %, 2.7 %, 1.7 %, 0.9 %, 0.6 % respectively to the total Hirshfeld surface area. Spikes arise in the fingerprint plots showing greater intermolecular interactions in the crystal packing of both **I** and **IV**.

3.4. 3D energy frameworks analysis

Energy framework analysis reveals the quantitative study of interaction energies and supramolecular design of molecules in a crystal. A cluster of molecules within 3.8 Å of the radius was built around a single **I** and **IV** compound. The scale factors used for developing the energy framework for B3LYP/6-31G(d,p) electron densities are k_ele = 1.057, k_pol = 0.740, k_disp = 0.871, k_rep = 0.618 (Edwards et al., 2017). Table 1 summarizeso the computed interaction energies in kJ/mol and the symmetry operations for eight molecules of **I**. The blue-colored molecule positioned at 10.44 Å has the greatest total interaction energy (-74.7 kJ/mol), whereas the green-colored one positioned at 10.09 Å has the lowest total interaction energy (0.9 kJ/mol). Similarly, as shown in Table 1, the computed energy interactions and symmetry operations for seven **IV** molecules are also given in kJ/mol.

S-axis is shown in Fig. 5. The Coulomb interactions in **I** look to be comparable in strength as R values are closer for both. The calculated interaction energies for electrostatic, polarization, dispersion, and repulsion of **I** are −111.0, −31.0, −173.1, and 176.6 kJ/mol, respectively. The calculated interaction energies for electrostatic, polarization, dispersion, and repulsion of *C*2 are −194.4, −53.1, −235.8, and 299.4 kJ/mol, respectively. The total energies of **I** and **IV** are −182.1 and −265.2 kJ/mol respectively. The dispersion energy has the highest value among all interaction energies in **I** and **IV**, i.e., the dispersion interaction energy dominates over the electrostatic Coulomb interaction energy. This is because of the presence of the bromo group, which has a large electron cloud in each compound. The more electrons an atom or molecule has (the most polarizable), the stronger dispersion forces are. The scale factors for benchmarked energies used for the construction of energy models were taken from Mackenzie *et al.* (Mackenzie et al., 2017).

The visualization of different interaction energies like Coulomb interaction energy, dispersion energy, and total interaction energy is represented by red, green, and blue colors, respectively, for the compounds, **I** and **IV** along different axes as shown in Fig. 6. The cylinders in the energy framework represent the relative strengths of molecular packing in several directions. An overall scale factor is used to contract or expand the size of the cylinders in the framework (Turner et al., 2015). There is an absence of cylinders in a particular direction due to the exclusion of a few interactions under certain threshold energy. These weaker interactions have been ignored only to make the figures less crowded.

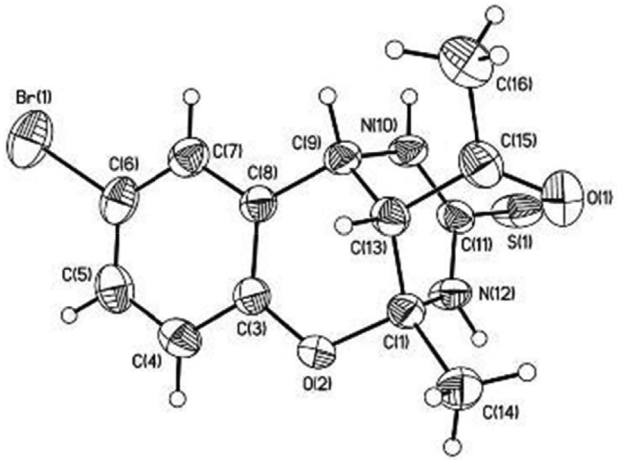

Fig. 2 Structure of **IV** according to the X-ray diffraction data.

3.5. Structure optimization

The synthesized compounds (**I** and **IV**) are optimized at the B3LYP/6-31G(d,p) level of theory using Gaussian 16 (Frisch et al., 2016) together with GuassView 6.0 (Dennington et al., 2016) and their fully optimized geometries are presented in Fig. 7.

3.6. Frontier molecular orbital (FMO) analysis

The FMO's of all compounds calculated at B3LYP/6-31G (d, p) DFT level are given in Fig. 8 along with values in Table 2.

The values of energy gaps for compounds **I** and **IV** are very close with a minor difference (5.050**,** 4.668 eV) as shown in Table 2. The compound **IV** shows a smaller ΔE value of 4.668 eV due to the greater π-conjugation than the **I** compound. Contrarily, the highest ΔE value of 5.050 eV is seen in **I**. Thus, the HOMO-LUMO energy gap shows the following

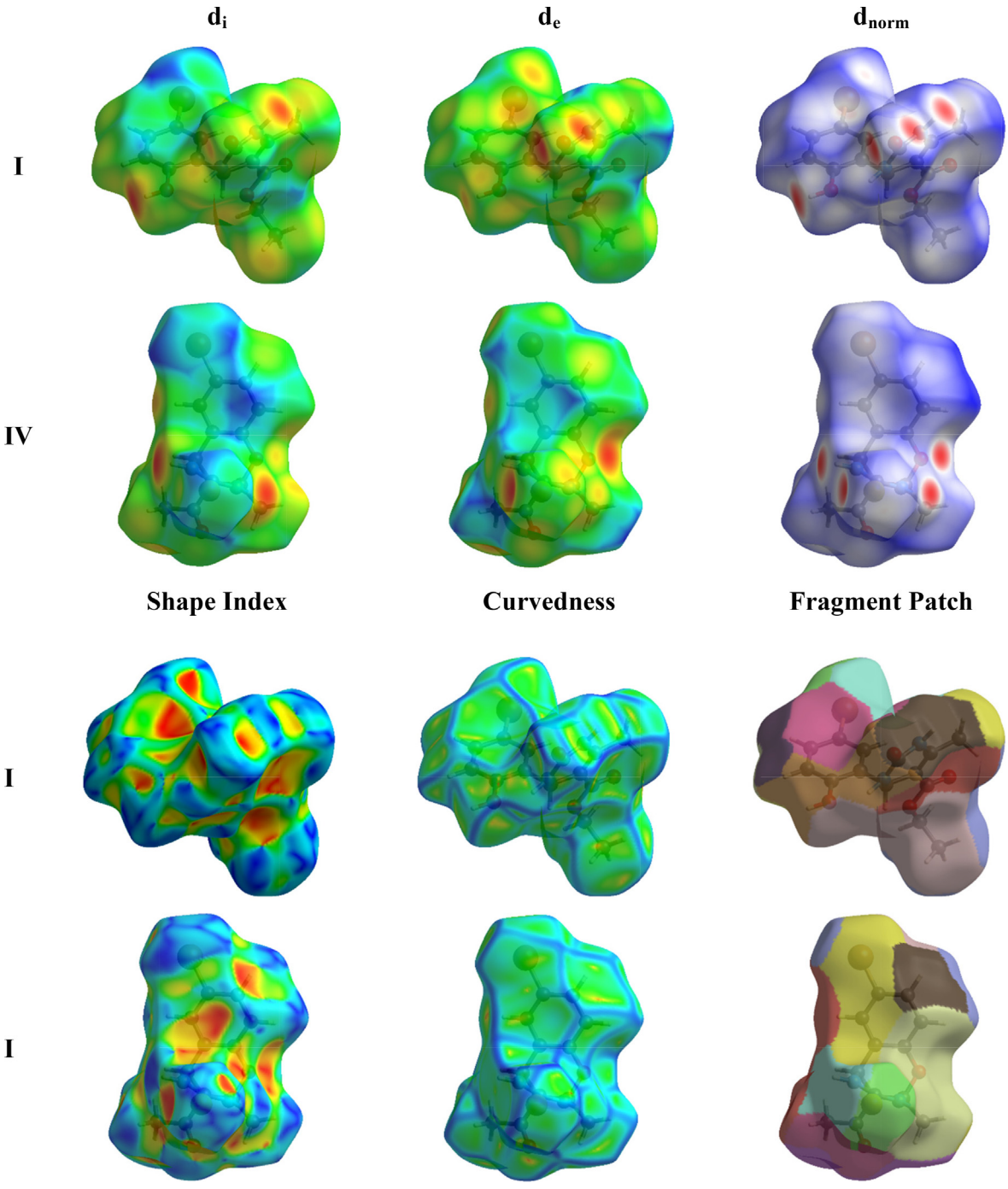

Fig. 3 Hirshfeld surface mapped of d_i, d_e, d_{norm}, curvedness, shape index, and fragment patch of compounds **I** and **IV**.

increasing order for all compounds: **IV** < **I**. The graphical diagrams are shown in Fig. 8 where red and yellow colors indicate the negative and positive phases of molecular orbitals, respectively.

3.7. Global reactivity descriptors

The ionization potential and electron affinity values in Table 3 illustrate that compound, **I**, show greater ionization potential than electron affinity revealing greater electron donating ability in comparison to the accepting nature. Overall, the electron affinity values are positive for both the compounds and a good gesture for their use in charge transfer reactions. The global electrophilicity values reveal that the electron donor capability (ω-) of these compounds are larger than the electron accepting capability (ω +). Similarly, the compound **IV** shows greater softness value followed by **I** with a minor difference. The electronegativity decreasing order observed among **I** and **IV** compounds is as **IV** > **I**. The synthesized compounds are harder

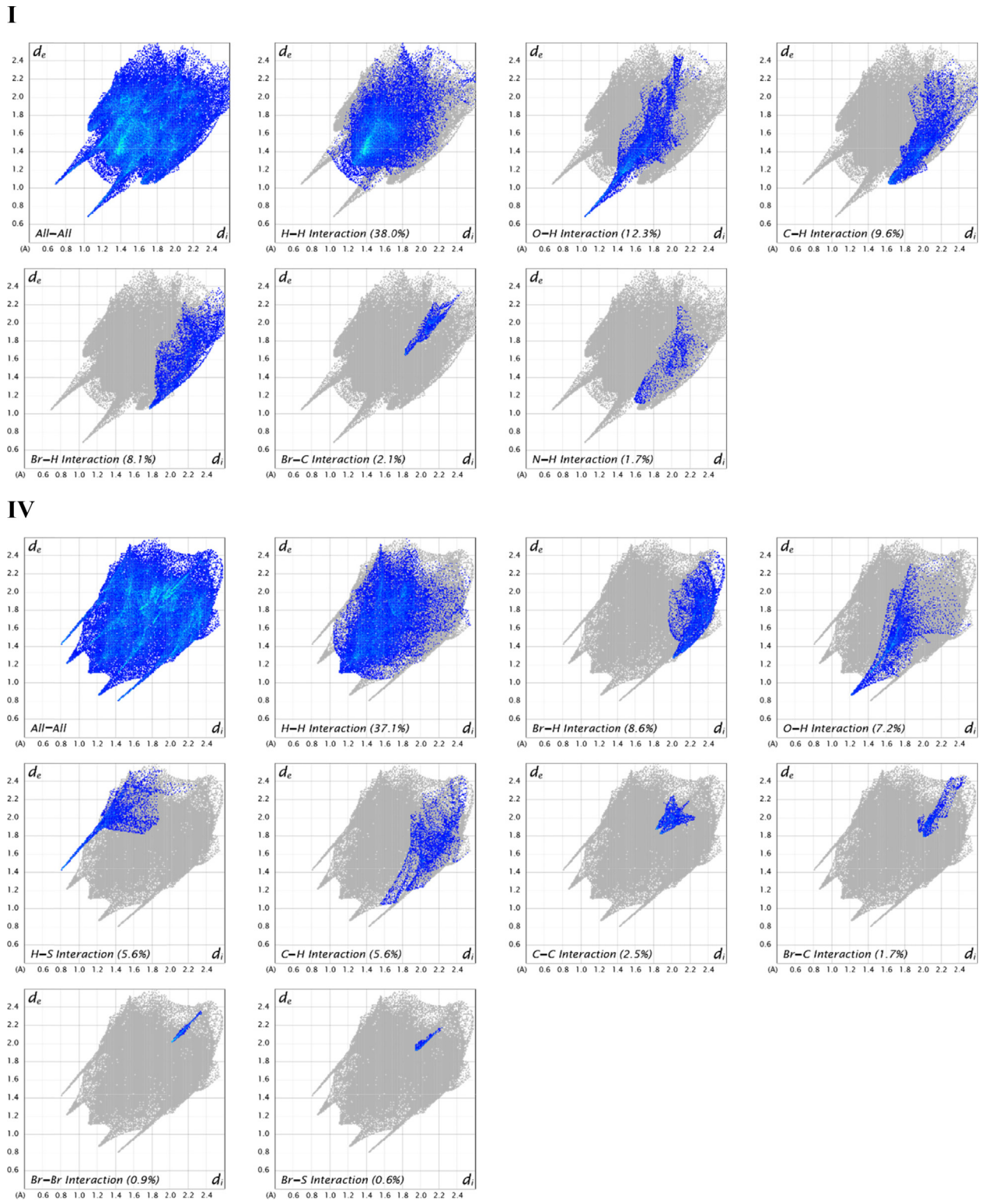

Fig. 4 2D fingerprint plots of **I** and **IV** displaying contacts for specific pairs of atoms contributing majorly.

due to large values of chemical hardness than the lower values of global softness.

These findings reveal a high degree of chemical stability and little reactivity. With the increase in the chemical potential (μ), chemical stability increases while reactivity decreases. The decrease in chemical potential for both the compounds is in the order: [**IV** (μ = -3.552) > **I** (μ = -3.548)]. This order indicates the lowest chemical potential (μ) for the compound **I** making it kinetically less stable and more reactive. Similarly, the molecules with smaller softness are less stable and more reactive.

Table 1 Interaction energies of the molecular pairs of **I** and **IV** in kJ/mol.

	N	Symmetry Operation	R	Electron Density	E_{ele}	E_{pol}	E_{dis}	E_{rep}	E_{tot}
I									
	1	x, y, z	9.32	B3LYP/6-31G(d,p)	−4.3	−1.0	−20.1	16.4	−12.7
	0	-x + 1/2, y + 1/2, -z + 1/2	8.49	B3LYP/6-31G(d,p)	−6.9	−1.5	−26.8	18.4	−20.5
	0	-x, -y, -z	12.42	B3LYP/6-31G(d,p)	−0.4	−0.2	−7.2	0.0	−6.9
	0	x, y, z	10.09	B3LYP/6-31G(d,p)	6.0	−1.3	−6.8	2.5	0.9
	1	x + 1/2, -y + 1/2, z + 1/2	8.60	B3LYP/6-31G(d,p)	−12.8	−2.6	−25.7	30.7	−18.8
	0	-x, -y, -z	10.44	B3LYP/6-31G(d,p)	−77.2	−20.0	−17.6	59.9	−74.7
	1	x + 1/2, -y + 1/2, z + 1/2	5.63	B3LYP/6-31G(d,p)	−13.2	−3.4	−60.8	46.1	−40.9
	0	-x, -y, -z	10.13	B3LYP/6-31G(d,p)	−2.2	−1.0	−8.1	2.6	−8.5
IV									
	1	-x, -y, -z	6.85	B3LYP/6-31G(d,p)	−40.8	−10.5	−54.1	69.8	−54.8
	1	x, -y, z + 1/2	9.4	B3LYP/6-31G(d,p)	−15.9	−5.1	−13.3	15.6	−22.5
	1	x, y, z	11.37	B3LYP/6-31G(d,p)	−0.3	−0.1	−4.4	2.2	−2.9
	1	x + 1/2, y + 1/2, z	10.16	B3LYP/6-31G(d,p)	−2.5	−2	−12	4.8	−11.6
	1	-x + 1/2, y + 1/2, -z + 1/2	8.73	B3LYP/6-31G(d,p)	−10.7	−4.4	−20.5	14	−23.7
	1	-x, y, -z + 1/2	4.89	B3LYP/6-31G(d,p)	−9.7	−5.7	−69	46.6	−45.8
	1	-x, -y, -z	6.53	B3LYP/6-31G(d,p)	−10.7	−2.1	−35.3	29	−25.7
	1	-x + 1/2, -y + 1/2, -z	10.24	B3LYP/6-31G(d,p)	0.5	−0.2	−2.4	0.1	−1.7
	0	-x + 1/2, -y + 1/2, -z	7.87	B3LYP/6-31G(d,p)	−105.8	−22.3	−19.1	116	−73.4
	1	x + 1/2, -y + 1/2, z + 1/2	9.76	B3LYP/6-31G(d,p)	1.5	−0.7	−5.7	1.3	−3.1

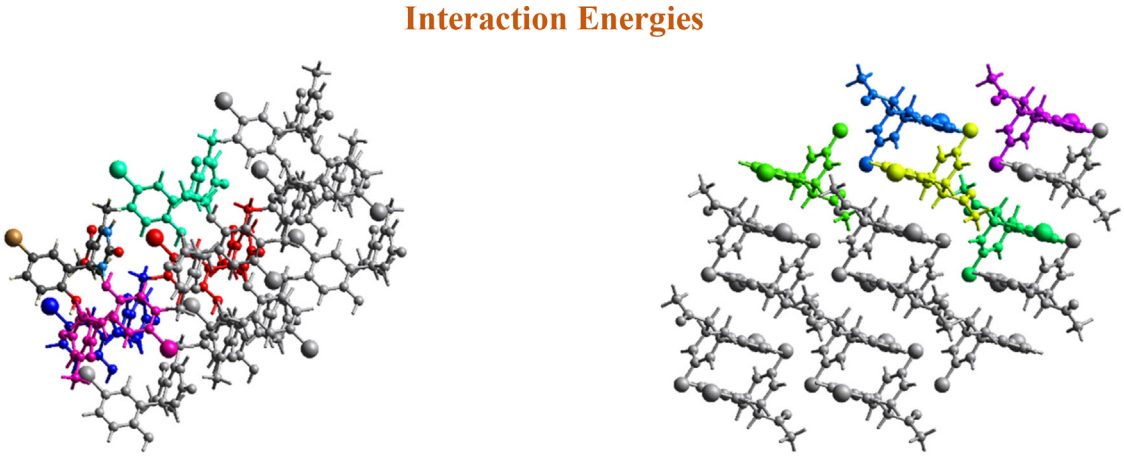

Fig. 5 Molecular pairs involved in the calculation of interaction energies of **I** and **IV** along the *b*-axis.

The results of the global reactivity parameters show both compounds have a higher donating potential, more stability, and a poorer accepting ability and thus are appropriate to participate in charge transfer reactions. Moreover, the purpose of performing DFT computation of these compounds is to endorse experimental studies, cross-check experimental findings, as well as to evaluate stability, reactivity, intramolecular or intermolecular charge transfer, and other parameters are suitable for predicting potential photovoltaic characteristics/biological activities (Pardasani et al., 2003; Pasha et al., 2007). Table 3 presents the global reactivity descriptors and accepting and donating aptitude of all compounds and endorses the relation with photovoltaic characteristics.

3.8. UV–visible study

To observe the electronic transitions, UV–vis spectroscopy is a powerful method, which also estimates the charge transfer probability in a compound and assignments of molecular orbitals corresponding to the transition (Siddique et al., 2021). Both, experimental and theoretical tools are used to study the UV–Visible transitions. The time-dependent DFT (TD-DFT) is performed at B3LYP functional in conjunction with the 6-31G(d,p) basis set.

Table 4 represents the absorption maxima, oscillator strength (*f*), and molecular assignments. Both experimental and theoretical absorption values are close to each other with minute differences. The compound **I** shows maximum absorption at 267.3 nm with an oscillator strength of 0.217 which is nearly equal to the experimental λ^{max} of 267.4 nm. Compounds **IV** shows absorption maxima at 247.8 nm bearing a very small difference with oscillator strengths of 0.210. Overall, the computed UV–vis studies are in fine contract with experimental absorption values. The HOMO to LUMO transition is the characteristic of photovoltaic materials, ΔE gap and chemical hardness indicate molecules are a little bit harder requiring

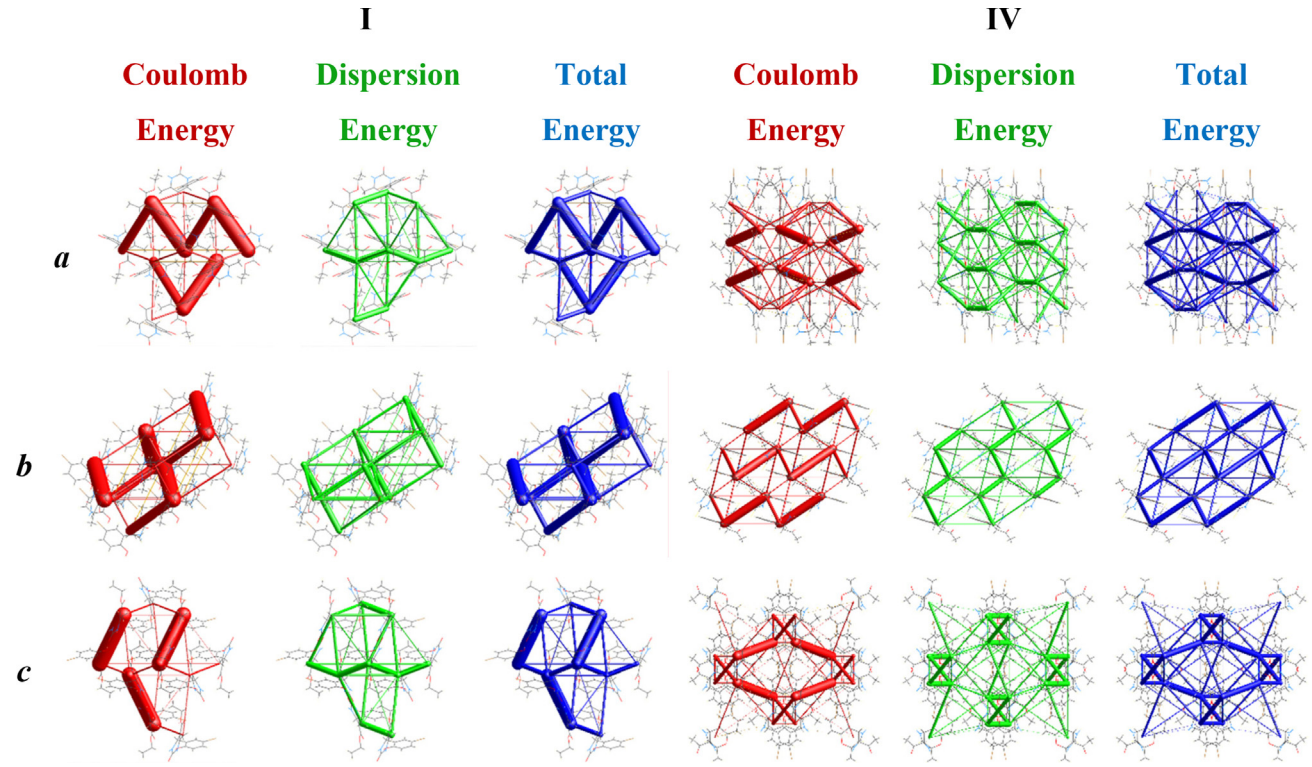

Fig. 6 The graphical representation of electrostatic interactions: Coulomb interaction energy (red), dispersion energy (green), and total interaction energy (blue) of **I** and **IV** along a, b, and c axes.

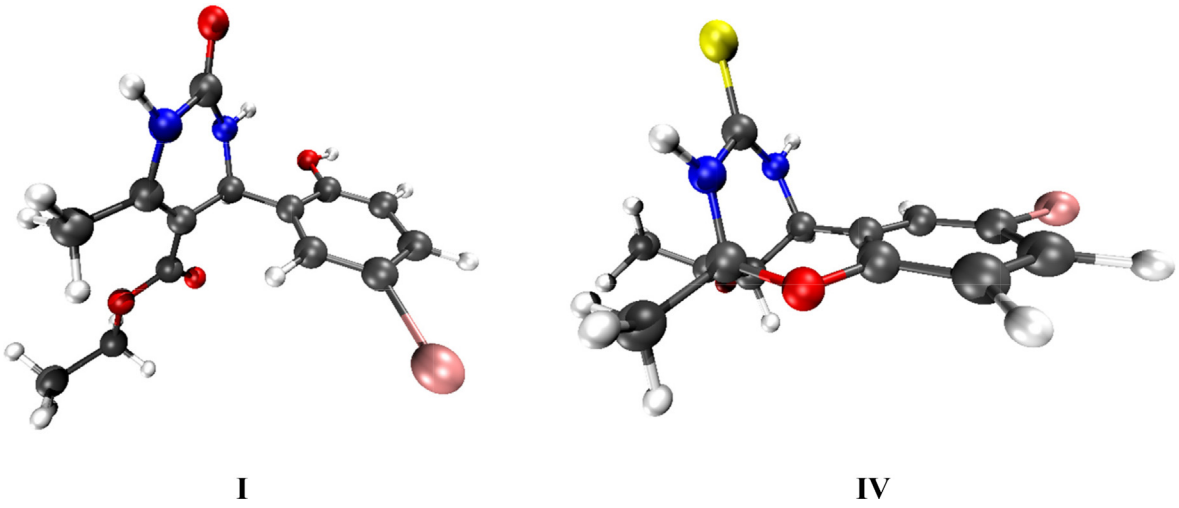

Fig. 7 Optimized geometries of **I** and **IV** compounds at B3LYP/6-31G(d,p) level of theory.

a large amount of energy for reactivity which is an indication of kinetic stability. The biological charge transfer and photovoltaic capability of C1 and *C*2 are in the order **IV** > **I** making them potential candidates.

3.9. Molecular electrostatic potential (MEP) analysis

The 3D representation of electron density on all compounds is explored via MEP analysis following equation (1).

$$V(\boldsymbol{r}) = \sum\nolimits_{A} \frac{\boldsymbol{Z_A}}{\boldsymbol{R_A} - \boldsymbol{r}} \int \frac{\boldsymbol{\rho}(\boldsymbol{r})\boldsymbol{dr'}}{\boldsymbol{r'} - \boldsymbol{r}} \tag{1}$$

Here, $V(r)$ is molecular electrostatic potential, Z_A is charge density over the nucleus, A placed at RA, $p(r')$ defines the electronic density function, and r' is the integration variable (Muthu and Prabhakaran, 2014; Okulik and Jubert, 2005).

The blue and red colors are the indications of nucleophilic and electrophilic centers, respectively. The magnitude of electrostatic potential is increased in order of

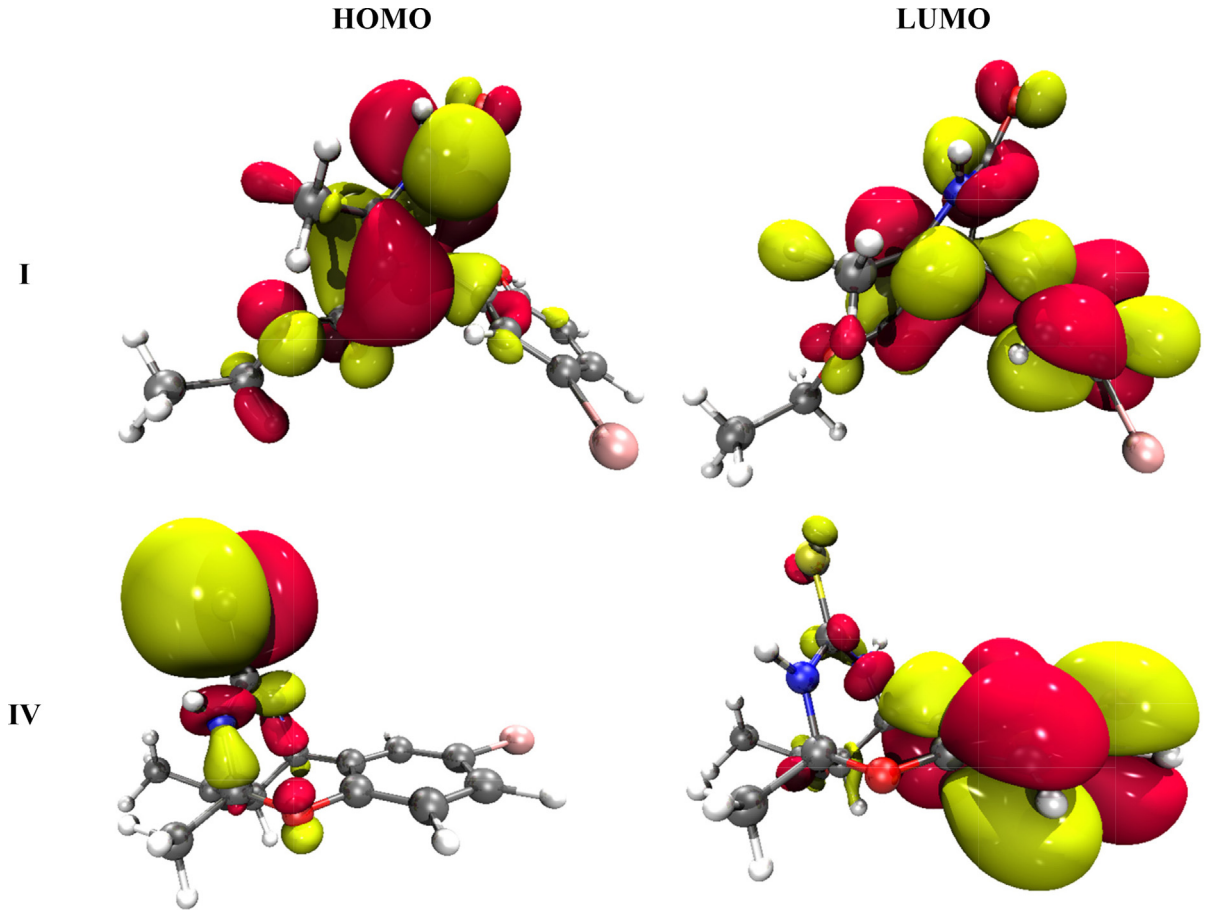

Fig. 8 The HOMO and LUMO pictorial representation of **I** and **IV** synthesized compounds.

Table 2 HOMO, LUMO energies, and Energy gap observed at B3LYP/6-31G(d,p) level.

Compounds	E_{HOMO} (eV)	E_{LUMO} (eV)	$\Delta E = E_{LUMO} - E_{HOMO}$ (eV)
I	−6.095	−1.045	5.050
IV	−5.806	−1.137	4.668

red < white < blue (Mahalakshmi and Balachandran, 2015). The electrophilic attack is easy on the red site while the blue site facilitates the nucleophilic attack. The 3D-MEP analysis is performed at B3LYP/6-31G(d,p) functional of all synthesized compounds and pictorial representation is given in Fig. 9. The oxygen, nitrogen, and sulfur atoms show negative potential (blue color), while mostly hydrogen and partially carbon and bromine atoms exhibit positive potential (red color). The white color indicates the mean potential being between two boundaries. The red and blue colors represent the different reaction sites.

3.10. NBO analysis

The charge transfer interactions within the bonds are studied using the natural bond orbital (NBO) analysis. The estimate of the off-diagonal NBO Fock matrix elements F(i,j) is given by this interaction energy. This could be calculated using the second-order perturbation method (Foster and Weinhold, 1980; Glendening et al., 1998). The one-center lone pairs and two-center bonds from NBO analysis show a precise representation of chemical bonding for a stable molecular species, which corresponds to a single Lewis structure. The non-Lewis set involves unoccupied valence nonbonding (LP^*) and

Table 3 Global reactivity descriptors of synthesized compounds at the B3LYP/6-31G(d,p) levels.

Compounds	Ionization Potential	Electron Affinity	Electronegativity	Hardness	Chemical Potential	Electrophilicity	e^- donor capability	e^- acceptor capability	softness
	I (eV)	A (eV)	χ (eV)	η (eV)	μ (eV)	ω (eV)	ω- (eV)	ω+ (eV)	S (eV)
I	7.674	−0.578	3.548	4.126	−3.548	1.526	3.815	0.267	0.121
IV	7.592	−0.488	3.552	4.040	−3.552	1.561	3.842	0.290	0.124

Table 4 Absorption values (λ^{max}), oscillator strength (*f*), and molecular assignments are obtained at TD-DFT/B3LYP/6-31G (d,p) level of DFT in chloroform solvent.

DFT λ^{max} (nm)	Exp. λ^{max} (nm)	*f* (oscillator strength)	MO contributions
267.3	267.4	0.217	H-1 → L (86 %) H-2 → L (4 %), H-1 → L + 1 (3 %), H → L (2 %)
247.8	248.9	0.210	H-2 → L + 1 (53 %), H-1 → L + 2 (12 %), H → L + 2 (27 %)

extra-valence-shell Rydberg (RY^*) orbitals also with the valence anti-bonds (BD^*). The shortfall of the Lewis-type NBOs (bonds and lone pairs) denoting the density matrix can be computed with the occupancy of these NBOs. The delocalization energy, *Eij*, is calculated as:

$$\boldsymbol{E}(2) = \boldsymbol{Eij} = \boldsymbol{qi}\frac{\boldsymbol{F}(\boldsymbol{i},\boldsymbol{j})^2}{(\boldsymbol{\varepsilon j} - \boldsymbol{\varepsilon i})} \quad (2)$$

Where *E(2)* is the energy of hyper conjugative interactions, *qi* is the occupancy of the contributing (Lewis type) orbital, εi and εj are the energies of the donating and accepting orbitals, and *Fij* is the off-diagonal element of the Fock matrix in the NBO basis (Frisch et al., 2000; Kleinman, 1962). An NBO analysis has been carried out to define the interior of the intramolecular hybridization and delocalization of electron density within the molecule.

Intermolecular hyper conjugative interactions are formed by overlapping the orbitals between the bonds of **I** (C—H), (C—O), (N—H), (C—C) and **IV** (C—H), (C—O), (C—N), (C—S), (C—C) and anti-bonding of **I** (C—C), (C—O), (C—N), (C–Br), (N—C) and **IV** (C—C), (C—S), (C—N), (C—O), (N—C), (C—H) orbitals, which result in intramolecular charge transfer (ICT) stabilizing the molecular system and leading to strong delocalization. The strong intramolecular hyper conjugative interactions of the electrons of **I** (C—H), (C—O), (N—H), (C—C), and **IV** (C—H), (C—O), (C—N), (C—S), (C—C) and anti-bonding of **I** (C—C), (C—O), (C—N), (C–Br), (N—C) and **IV** (C—C), (C—S), (C—N), (C—O), (N—C), (C—H) bonds of the ring lead to stabilization of some part of the ring as given in Table 5. For example, in **I**, the intermolecular hyper conjugative interaction of σ (N2–H22) distributes to σ* (C1–N6) and in **IV** σ (C15–S16) distributes to σ* (C15–S16), leading to stabilization of 21.129 KJ/mol and 10.91 KJ/mol, respectively.

This enhanced further conjugation with an anti-bonding orbital of **I** π (C4–C5) and **IV** π (C4–C5) which led to a strong delocalization of 98.742 KJ/mol and 23.24 KJ/mol with π^* (C7–O8) in C1 and π* (C1–C6) in **IV**, respectively. The most important highest energy, related to molecule **I**, is electron-donating from π* (C13–C14) to the anti-bonding acceptor π* (C12–C17) and for *C*2, electron-donating from π* (C1–C6) to the anti-bonding acceptor π* (*C*2–C3) with stabilization energies of 845.796 and 204.94 KJ/mol, respectively. The magnitude of charge transferred in C1 from LP (2) O9 to the anti-bonding π* (C7–O8) and LP (1) N2 to the anti-bonding π* (C1–O10) shows that the stabilization energy is 6.38 KJ/mol and 10.89 KJ/mol, respectively. Similarly, in *C*2, the charge transferred from LP (1) N14 to the anti-bonding σ* (C15–S16) and LP (2) O8 to the anti-bonding π* (C4–C5) with stabilization energies of 52.70 and 28.53 KJ/mol, respectively.

3.11. Optical properties

Nonlinear optical materials may find use in optoelectronic devices, networking, signal manipulation, telecommunications, and other fields. The strength of the donor–acceptor group, as well as the sequence in which they are placed, affects the amount of nonlinear optical efficiency. To put it another way, organic NLO materials have a push–pull conjugated structure because of the π-electron conjugated system they contain, bearing electron donor and acceptor groups on different ends. The present work has been extended to explore the optical properties of the **I** and **IV** complexes for their remarkable utilization in optoelectronic. The optoelectronics properties include dipole moment (μ_{tot}), polarizability (α_{tot}), and first-order hyperpolarizability (β_{tot}) (Kurtz et al., 1990) and are determined by the following equations:

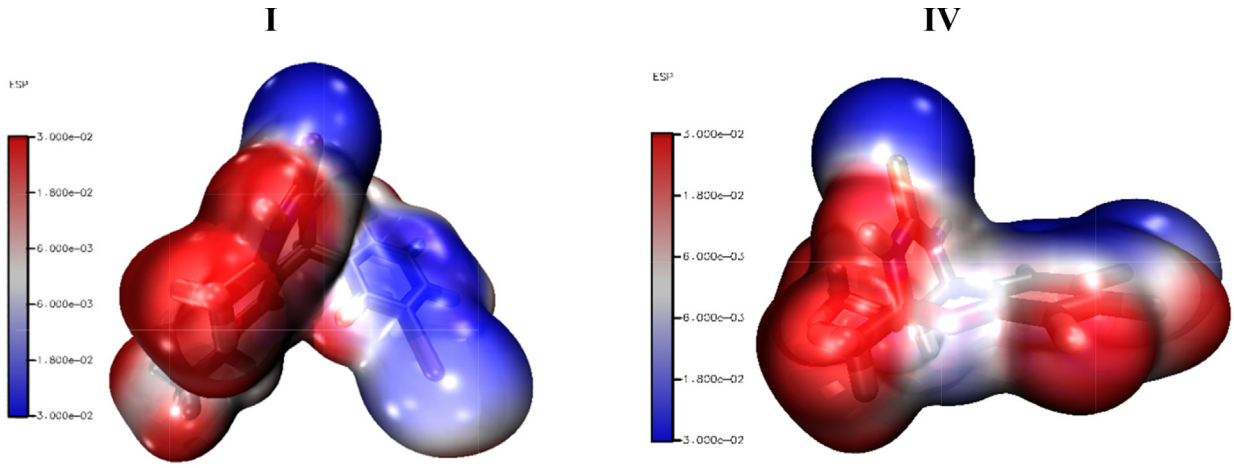

Fig. 9 The 3D MEP representation of **I** and **IV** at B3LYP/6-31G(d,p) level of DFT.

Table 5 Second-order perturbation theory analysis of Fock matrix in NBO basis of **I** and **IV** compounds.

I					
Donor (i)	**Acceptor (j)**	**E(2) kJ/mol**	**E(2) kcal/mol**	**E(j)-E(i) a.u.**	**F(i,j) a.u.**
π* C13 - C14	π* C12 - C17	845.796	202.15	0.02	0.083
LP (2) O9	π* C7 - O8	189.703	45.34	0.33	0.112
LP (1) N2	π* C1 - O10	182.632	43.65	0.33	0.109
LP (2) O8	σ* C7 - O9	139.369	33.31	0.62	0.13
π C4 - C5	π* C7 - O8	98.742	23.6	0.29	0.077
π* C1 - O10	σ* C1 - O10	56.2748	13.45	0.49	0.167
LP (3) Br19	π* C15 - C16	38.618	9.23	0.3	0.052
σ N2 - H22	σ* C1 - N6	21.129	5.05	1.05	0.066
σ* C7 - O9	σ* C3 - C4	20.83632	4.98	0.04	0.05
σ C14 - C15	σ* C16 -Br19	20.502	4.9	0.79	0.056
σ C11 - H25	π* C4 - C5	20.334	4.86	0.55	0.049
σ N6 - H24	σ* C1 - N2	15.397	3.68	1.14	0.059
π C1 - O10	π* C1 - O10	8.619	2.06	0.48	0.031
π* C12 - C17	σ* N2 - C3	8.28432	1.98	0.31	0.052
σ C20 - H33	RY*(2) O9	2.803	0.67	1.63	0.029
IV					
π* C1 - C6	π* C2 - C3	204.94	0.01	0.08	857.469
LP (1) N14	σ* C15 - S16	52.70	0.25	0.107	220.497
LP (2) O8	π* C4 - C5	28.53	0.34	0.094	119.370
π C4 - C5	π* C1 - C6	23.24	0.28	0.073	97.236
σ* C15 - S16	π* C15 - S16	14.47	0.27	0.109	60.542
LP (2) S16	σ* N13 - C15	11.09	0.62	0.075	46.401
σ C15 - S16	σ* C15 - S16	10.91	0.29	0.057	45.647
LP (3) Br7	π* C1 - C6	9.53	0.3	0.052	39.874
σ C19 - H32	π* C17 - O18	6.66	0.52	0.053	27.865
σ C11 - N14	π* C15 - S16	3.35	1	0.052	14.016
π* C4 - C5	σ* C11 - N14	3.31	0.3	0.059	13.849
σ C4 - O8	RY*(1) C9	2.7	1.84	0.063	11.297
π* C2 - C3	RY*(5) C2	1.79	1.14	0.1	7.489
π C17 - O18	σ* C19 - H32	1.66	0.81	0.033	6.945
σ C17 - C19	RY*(1) C10	1.41	1.63	0.043	5.899

$$\mu_{tot} = \left(\mu_x^2 + \mu_y^2 + \mu_z^2\right)^{1/2} \quad (3)$$

$$\alpha_{tot} = \frac{1}{3}\left(\alpha_{xx} + \alpha_{yy} + \alpha_{zz}\right) \quad (4)$$

$$\beta_{tot} = \left[\beta_x{}^2 + \beta_y{}^2 + \beta_z{}^2\right]^{1/2} \quad (5)$$

The first hyperpolarizability is a third rank tensor with a 3 × 3 × 3 matrix, and the 27 components of the 3D matrix are reduced to 10 components due to the Kleinman symmetry. The dipole moment, linear polarizability, and nonlinear first hyperpolarizability of the **I** and **IV** are listed in Table 6. The dipole moments of **I** and **IV** are 1.543 D and 4.504 D, respectively. The polarizabilities of **I** and **IV** are 188.2 au and 186.1 au, respectively. The results clearly show that the largest component of polarizability is along the axial direction, whereas perpendicular components contribute minimally, indicating that the molecule is optically active in the X-direction. The first-order hyperpolarizabilities of **I** and **IV** are 526.5 au and 427.6 au. The greater hyperpolarizability of **I** than **IV** is mainly attributed to the greater intramolecular charge transfer between different atoms of **I**. Besides this, the NLO response of **I** and **IV** is larger than the reference molecule urea (Kanis et al., 1994), which has a total value of 43 au, indicating that these complexes can be potential NLO candidates for optoelectronic applications.

3.12. Molecular docking study

The docking was conducted to examine the binding affinity of compounds with different targets of the SARS-CoV-2 virus. Of the different targets used, it was found the main protease enzyme was the best-docked enzyme for the compounds used, as shown in Table 7. Compound **I** had binding energy of −12.67 kcal/mol for the SARS-CoV-2 main protease enzyme, while compound **IV** had binding energy of −11.24 kcal/mol. Both the compounds dock well inside the binding cavity of the enzyme and are engaged by hydrophilic and hydrophobic interactions. The compound **I** formed hydrogen bonds with Asn142, Ser144, and Gly143. Similarly, compound **IV** formed hydrogen bonds with Phe 140, Gly143, and Cys145. The binding mode and chemical interactions of the compounds with the enzyme are given in Fig. 10.

3.13. Molecular dynamics simulation

As the compounds showed stronger binding affinity with the SARS-CoV-2 main protease enzyme compared to others, only main protease enzyme compounds best docked complexes were subjected to molecular dynamics simulation analysis. According to the molecular dynamic simulations, compound **I** is more dynamically stable compared to compound **IV**. The

Table 6 Dipole moment (Debye), polarizability (au), and nonlinear first order hyperpolarizability (au) of C1 and *C*2 complexes.

I				**IV**			
Dipole moment (Debye)		**Hyperpolarizability (au)**		**Dipole moment (Debye)**		**Hyperpolarizability (au)**	
Parameter	**Value**	**Parameter**	**Value**	**Parameter**	**Value**	**Parameter**	**Value**
μ_x	1.543	β_{xxx}	15.49	μ_x	0.000	β_{xxx}	73.29
μ_y	0.000	β_{yyy}	29.25	μ_y	0.000	β_{yyy}	24.19
μ_z	0.000	β_{zzz}	479.7	μ_z	4.504	β_{zzz}	133.1
μ_{tot}	1.543	β_{xyy}	50.63	μ_{tot}	4.504	β_{xyy}	32.06
Polarizability (au)		β_{xxy}	87.27	**Polarizability (au)**		β_{xxy}	−114.8
α_{xx}	191.6	β_{xxz}	−17.42	α_{xx}	226.9	β_{xxz}	106.1
α_{xy}	7.690	β_{xzz}	229.7	α_{xy}	−20.52	β_{xzz}	77.00
α_{xz}	−15.34	β_{yzz}	−69.17	α_{xz}	−15.14	β_{yzz}	−94.06
α_{yy}	202.2	β_{yyz}	−29.24	α_{yy}	161.1	β_{yyz}	100.6
α_{yz}	−8.241	β_{xyz}	66.00	α_{yz}	11.33	β_{xyz}	−53.14
α_{zz}	170.7	β_{tot}	526.5	α_{zz}	170.3	β_{tot}	427.6
α_{tot}	188.2			α_{tot}	186.1		

Table 7 Docking score of compounds with different SARS-CoV-2 targets. The energy value is in kcal/mol.

Compound	**Main Protease Enzyme**	RdRp Enzyme	**E Protein**
Compound I	−12.67	−6.35	−7.65
Compound IV	−11.24	−5.65	−6.65

root means square deviation (RMSD) reached a maximum level of 2 Å. The compound **IV**, on the other hand, showed significant deviation (up to 7 Å) in the first 100 ns. Followed that, the complex was found very stable towards the end of the simulation. The residue-wise fluctuations were measured via the root mean square fluctuation (RMSF), which indicated that in the presence of compound **I,** the enzyme remained very stable compared to compound **IV**. The RMSD and RMSF of compounds are given in Fig. 11**.**

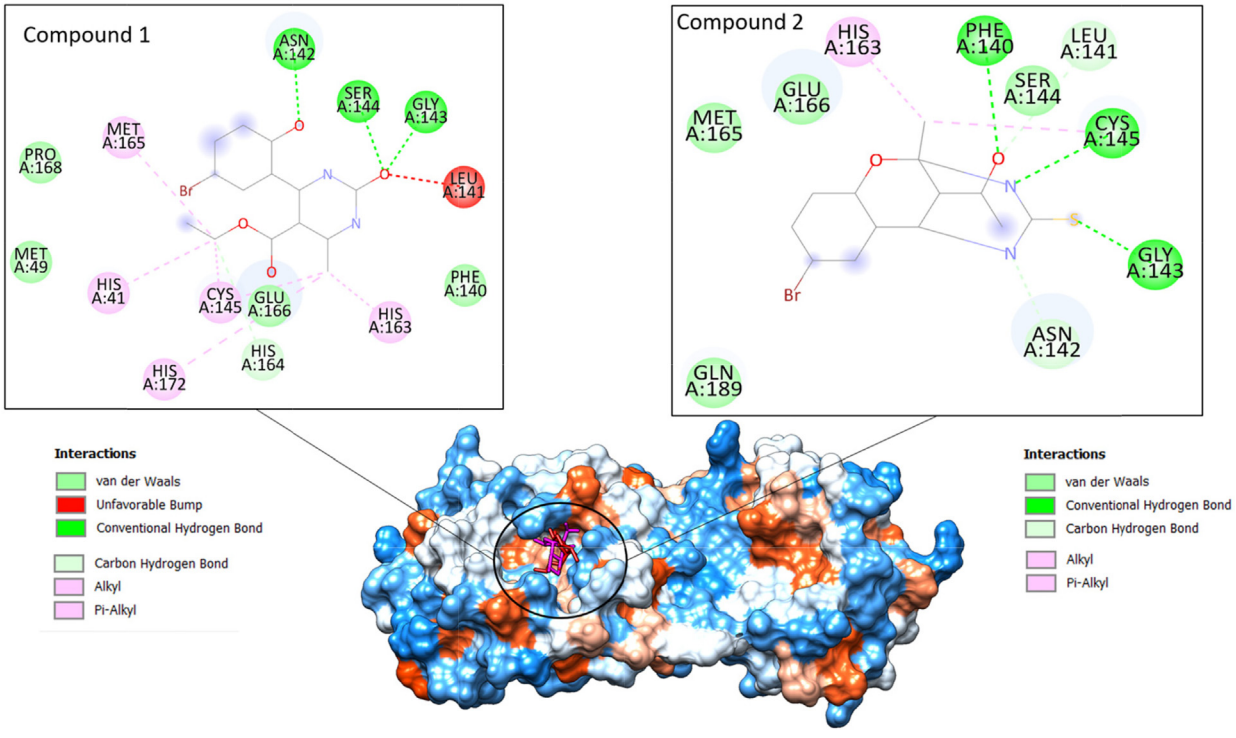

Fig. 10 Binding of the compounds at substrate binding cavity of SARS-CoV-2 main protease enzyme. Compound **I** is shown by a red stick while compound **IV** is pink. The enzyme is on hydrophobicity surface. The binding interactions of compounds are also given.

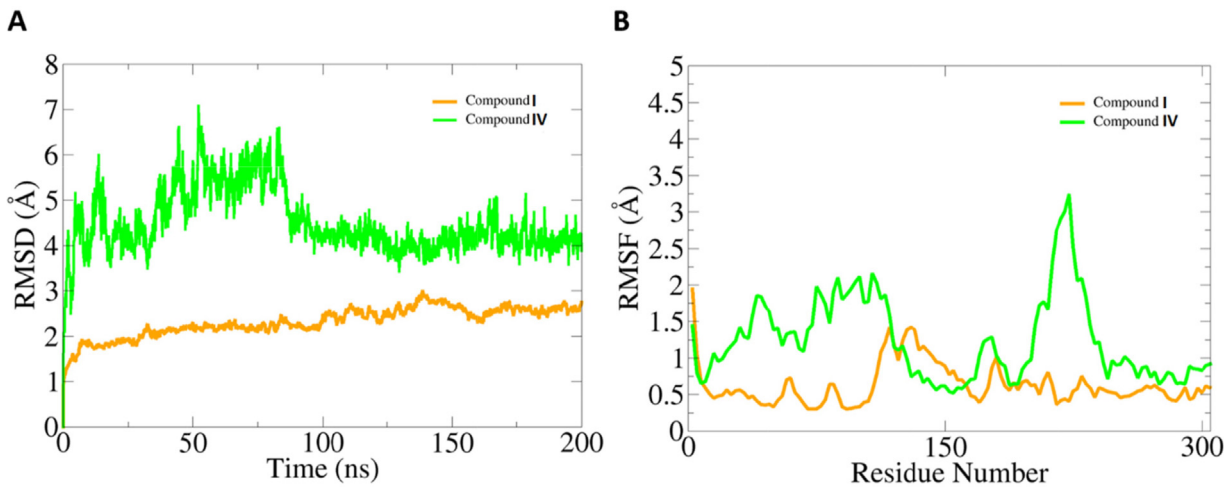

Fig. 11 Dynamics investigation of compounds with SARS-CoV-2 main protease enzyme. **A.** RMSD and **B.** RMSF. Both values are measured in Å.

Table 8 Atomic-level interaction energies are given in kcal/mol.

Parameter	Compound I Complex	Compound IV Complex
MMGBSA		
Van der Waals Energy	−55.36	−43.88
Electrostatic Energy	−25.41	−19.18
Polar Solvation Energy	35.13	29.03
Non-Polar Solvation Energy	−13.36	−12.66
Net Energy	−59	−46.69
MMPBSA		
Van der Waals Energy	−55.36	−43.88
Electrostatic Energy	−25.41	−19.18
Polar Solvation Energy	33.497	32.04
Non-Polar Solvation Energy	−12.28	−10.04
Net Energy	−59.553	−41.03

3.14. MMPB\GBSA analysis

Different binding free energies of the compounds with the enzyme active site residues were also estimated. Again, compound **I** was ranked as the best-docked molecule with the main protease enzyme. The binding free energies of compounds are tabulated in Table 8. The net binding free energy of compound **I** is −59 kcal/mol in MMGBSA and −59.553 kcal/mol in MMPBSA. The energy value of compound **I** is better than that of compound **IV,** which has a net energy of −46.69 kcal/mol in MMGBSA and net energy of −41.03 kcal/mol in MMPBSA.

4. Conclusions

In this paper, we carried out several computation analyses to treat test dihydropyrimidines due to the possible benefits that can hit today's prominent pandemic problem.

Furthermore, from the DFT theoretical calculations, the optimized geometrical parameters are analyzed and are in good agreement with the XRD results. We found that the HOMO-LUMO energy gap affects the stability of compounds. Similarly, NBO and natural atomic charge analyses were performed to explore the stabilization energy of different inter- and intramolecular interactions within the systems and the net charge distribution, respectively. Insights from the DFT study of these compounds reveal their good stability by using other analyses like global indices of reactivity and molecular electrostatic potential analysis. Molecular docking and MD simulations were used to assess the binding affinity and stability of these drugs to the binding site of the SARS-CoV-2 receptor. Through molecular docking studies with various types of interactions, substantial binding affinity for both examined compounds was established. Following the computational techniques, the substrates were subjected to MD simulations to measure the rigidity of the protein structure, fluctuations caused by interactions, and overall structural stability by calculating RMSD.

Declaration of Competing Interest

The authors declare that they have no known competing financial interests or personal relationships that could have appeared to influence the work reported in this paper.

Appendix A. Supplementary material

Supplementary data to this article can be found online at https://doi.org/10.1016/j.arabjc.2022.104230.

References

Ashok, M., Holla, B.S., Kumari, N.S., 2007. Convenient one-pot synthesis of some novel derivatives of thiazolo [2, 3-b] dihydropyrimidinone possessing 4-methylthiophenyl moiety and evaluation of their antibacterial and antifungal activities. Eur. J. Med. Chem. 42, 380–385.

Bais, J., Benedetti, F., Berti, F., Cerminara, I., Drioli, S., Funicello, M., Regini, G., Vidali, M., Felluga, F., 2020. One pot synthesis of micromolar BACE-1 inhibitors based on the dihydropyrimidinone scaffold and their thia and imino analogues. Molecules 25, 4152.

Biovia, D.S., 2017. Discovery studio visualizer. San Diego, CA, USA.

Case, D.A., Belfon, K., Ben-Shalom, I., Brozell, S.R., Cerutti, D., Cheatham, T., Cruzeiro, V.W.D., Darden, T., Duke, R.E., Giambasu, G., others, 2020. Amber 2020.

Chiang, A.N., Valderramos, J.-C., Balachandran, R., Chovatiya, R.J., Mead, B.P., Schneider, C., Bell, S.L., Klein, M.G., Huryn, D.M., Chen, X.S., 2009. Select pyrimidinones inhibit the propagation of the malarial parasite, Plasmodium falciparum. Bioorg. Med. Chem. 17, 1527–1533.

Chitra, S., Devanathan, D., Pandiarajan, K., 2010. Synthesis, Spectral, Anti-Liver Cancer and Free Radical Scavenging Activity of New Azabicyclic Thienoyl Hydrazone Derivatives. Eur. J. Med. Chem 45, 367–371.

Cousins, K.R., 2011. Computer review of ChemDraw ultra 12.0.

de Fátima, Â., Braga, T.C., Neto, L. da S., Terra, B.S., Oliveira, B.G. F., da Silva, D.L., Modolo, L. V, 2015. A mini-review on Biginelli adducts with notable pharmacological properties. J. Adv. Res. 6, 363–373

Dennington, R., Keith, T.A., Millam, J.M., 2016. GaussView 6.0. 16. Semichem Inc. Shawnee Mission. KS, USA.

Deshmukh, M.B., Salunkhe, S.M., Patil, D.R., Anbhule, P.V., 2009. A novel and efficient one step synthesis of 2-amino-5-cyano-6-hydroxy-4-aryl pyrimidines and their anti-bacterial activity. Eur. J. Med. Chem. 44, 2651–2654.

Edwards, A.J., Mackenzie, C.F., Spackman, P.R., Jayatilaka, D., Spackman, M.A., 2017. Intermolecular interactions in molecular crystals: what's in a name? Faraday Discuss. 203, 93–112.

Foster, J.P., Weinhold, F., 1980. Natural hybrid orbitals. J. Am. Chem. Soc. 102 (24), 7211–7218.

Frisch, M.J., Trucks, G.W., Schlegel, H.B., Scuseria, G.E., Robb, M. A., Cheeseman, J.R., Scalmani, G., Barone, V., Petersson, G.A., Nakatsuji, H., 2016. Gaussian 16.

Frisch, A., Nielson, A.B., Holder, A.J., 2000. Gaussview user manual. Gaussian Inc., Pittsburgh, PA, p. 556.

Genheden, S., Ryde, U., 2015. The MM/PBSA and MM/GBSA methods to estimate ligand-binding affinities. Expert Opin. Drug Discov. 10, 449–461. https://doi.org/10.1517/17460441.2015.1032936.

Gireesh, T., Kamble, R.R., Kattimani, P.P., Dorababu, A., Manikantha, M., Hoskeri, J.H., 2013. Synthesis of sydnone substituted Biginelli derivatives as hyaluronidase inhibitors. Arch. Pharm. (Weinheim) 346, 645–653.

Glendening, E.D., Reed, A.E., Carpenter, J.E., Weinhold, F., 1998. NBO Version 3.1. Google Sch. There is no Corresp. Rec. this Ref.

He, X., Liu, S., Lee, T.-S., Ji, B., Man, V.H., York, D.M., Wang, J., 2020. Fast, accurate, and reliable protocols for routine calculations of protein–ligand binding affinities in drug design projects using AMBER GPU-TI with ff14SB/GAFF. ACS Omega 5, 4611–4619.

Ismaili, L., Nadaradjane, A., Nicod, L., Guyon, C., Xicluna, A., Robert, J.-F., Refouvelet, B., 2008. Synthesis and antioxidant activity evaluation of new hexahydropyrimido [5, 4-c] quinoline-2, 5-diones and 2-thioxohexahydropyrimido [5, 4-c] quinoline-5-ones obtained by Biginelli reaction in two steps. Eur. J. Med. Chem. 43, 1270–1275.

Izaguirre, J.A., Catarello, D.P., Wozniak, J.M., Skeel, R.D., 2001. Langevin stabilization of molecular dynamics. J. Chem. Phys. 114, 2090–2098.

Kaliappan, S., Bombay, I.I.T., 2016. UCSF Chimera-Superimposing and Morphing.

Kanis, D.R., Ratner, M.A., Marks, T.J., 1994. Design and construction of molecular assemblies with large second-order optical nonlinearities. Quant. Chem. Asp. Chem. Rev. 94, 195–242.

Kaur, R., Chaudhary, S., Kumar, K., Gupta, M.K., Rawal, R.K., 2017. Recent synthetic and medicinal perspectives of dihydropyrimidinones: a review. Eur. J. Med. Chem. 132, 108–134.

Kaur, H., Machado, M., de Kock, C., Smith, P., Chibale, K., Prudêncio, M., Singh, K., 2015. Primaquine–pyrimidine hybrids: synthesis and dual-stage antiplasmodial activity. Eur. J. Med. Chem. 101, 266–273.

Khan, S., Kale, M., Siddiqui, F., Nema, N., 2021. Novel pyrimidine-benzimidazole hybrids with antibacterial and antifungal properties and potential inhibition of SARS-CoV-2 main protease and spike glycoprotein. Digit. Chinese Med. 4, 102–119.

Kidwai, M., Saxena, S., Khan, M.K.R., Thukral, S.S., 2005. Synthesis of 4-aryl-7, 7-dimethyl-1, 2, 3, 4, 5, 6, 7, 8-octahydroquinazoline-2-one/thione-5-one derivatives and evaluation as antibacterials. Eur. J. Med. Chem. 40, 816–819.

Kleinman, D.A., 1962. Nonlinear dielectric polarization in optical media. Phys. Rev. 126, 1977.

Kräutler, V., Van Gunsteren, W.F., Hünenberger, P.H., 2001. A fast SHAKE algorithm to solve distance constraint equations for small molecules in molecular dynamics simulations. J. Comput. Chem. 22, 501–508.

Kurbanova, M.M., 2010. Bicyclic compounds obtained by the Biginelli reaction. Russ. J. Org. Chem. 46, 599–601.

Kurbanova, M.M., Kurbanov, A.V., Askerov, R.K., Allakhverdiev, M.A., Khrustalev, V.N., Magerramov, A.M., 2009. Crystal structures of ethyl-4-(5-bromo-2-hydroxyphenyl)-6-methyl-2-oxo-1, 2, 3, 4-tetrahydropyrimidine-5-carboxylate and ethyl-1-methyl-15-oxo-2-oxa-14, 16-diazatetracyclo [11.3. 1.03. 12.06. 11] heptadeca-3, 5, 7, 9, 11-pentaene-17-carboxylate. J. Struct. Chem. 50, 505–509.

Kurtz, H.A., Stewart, J.J.P., Dieter, K.M., 1990. Calculation of the nonlinear optical properties of molecules. J. Comput. Chem. 11, 82–87.

Li, Y., Tan, T., Zhao, Y., Wei, Y., Wang, D., Chen, R., Tao, L., 2020. Anticancer polymers via the Biginelli reaction. ACS Macro Lett. 9, 1249–1254.

Liu, Y., Liu, J., Zhang, R., Guo, Y., Wang, H., Meng, Q., Sun, Y., Liu, Z., 2019. Synthesis, characterization, and anticancer activities evaluation of compounds derived from 3, 4-dihydropyrimidin-2 (1H)-one. Molecules 24, 891.

Mackenzie, C.F., Spackman, P.R., Jayatilaka, D., Spackman, M.A., 2017. CrystalExplorer model energies and energy frameworks: extension to metal coordination compounds, organic salts, solvates and open-shell systems. IUCrJ 4, 575–587.

Mahalakshmi, G., Balachandran, V., 2015. NBO, HOMO, LUMO analysis and vibrational spectra (FTIR and FT Raman) of 1-Amino 4-methylpiperazine using ab initio HF and DFT methods. Spectrochim. Acta Part A Mol. Biomol. Spectrosc. 135, 321–334.

Maier, J.A., Martinez, C., Kasavajhala, K., Wickstrom, L., Hauser, K. E., Simmerling, C., 2015. ff14SB: improving the accuracy of protein side chain and backbone parameters from ff99SB. J. Chem. Theory Comput. 11, 3696–3713.

Maity, T., Mandal, H., Bauzá, A., Samanta, B.C., Frontera, A., Seth, S.K., 2018. Quantifying conventional C-H$\cdots\pi$ (aryl) and unconventional C–H$\cdots\pi$ (chelate) interactions in dinuclear Cu (II) complexes: experimental observations, Hirshfeld surface and theoretical DFT study. New J. Chem. 42, 10202–10213.

McKinnon, J.J., Jayatilaka, D., Spackman, M.A., 2007. Towards quantitative analysis of intermolecular interactions with Hirshfeld surfaces. Chem. Commun., 3814–3816

Miller, B.R., McGee, T.D., Swails, J.M., Homeyer, N., Gohlke, H., Roitberg, A.E., 2012. MMPBSA.py: An efficient program for end-state free energy calculations. J. Chem. Theory Comput. 8, 3314–3321. https://doi.org/10.1021/ct300418h.

Mokale, S.N., Shinde, S.S., Elgire, R.D., Sangshetti, J.N., Shinde, D. B., 2010. Synthesis and anti-inflammatory activity of some 3-(4, 6-disubtituted-2-thioxo-1, 2, 3, 4-tetrahydropyrimidin-5-yl) propanoic acid derivatives. Bioorg. Med. Chem. Lett. 20, 4424–4426.

Muthu, S., Prabhakaran, A., 2014. Vibrational spectroscopic study and NBO analysis on tranexamic acid using DFT method. Spectrochim. Acta Part A Mol. Biomol. Spectrosc. 129, 184–192.

Nagarajaiah, H., Mukhopadhyay, A., Moorthy, J.N., 2016. Biginelli reaction: an overview. Tetrahedron Lett. 57, 5135–5149.

Okulik, N., Jubert, A.H., 2005. Theoretical analysis of the reactive sites of non-steroidal anti-inflammatory drugs. Internet Electron. J. Mol. Des. 4, 17–30.

Pardasani, R.T., Pardasani, P., Chaturvedi, V., Yadav, S.K., Saxena, A., Sharma, I., 2003. Theoretical and synthetic approach to novel spiroheterocycles derived from isatin derivatives and L-proline via 1, 3-dipolar cycloaddition. Heteroat. Chem. An Int. J. Main Gr. Elem. 14, 36–41.

Pasha, F.A., Neaz, M.M., Cho, S.J., Kang, S.B., 2007. Quantitative structure activity relationship (QSAR) study of estrogen derivatives based on descriptors of energy and softness. Chem. Biol. Drug Des. 70, 520–529.

Pettersen, E.F., Goddard, T.D., Huang, C.C., Couch, G.S., Greenblatt, D.M., Meng, E.C., Ferrin, T.E., 2004. UCSF Chimera—a visualization system for exploratory research and analysis. J. Comput. Chem. 25, 1605–1612.

Rajanarendar, E., Reddy, M.N., Murthy, K.R., Reddy, K.G., Raju, S., Srinivas, M., Praveen, B., Rao, M.S., 2010. Synthesis, antimicrobial, and mosquito larvicidal activity of 1-aryl-4-methyl-3, 6-bis-(5-methylisoxazol-3-yl)-2-thioxo-2, 3, 6, 10b-tetrahydro-1H-pyrimido [5, 4-c] quinolin-5-ones. Bioorg. Med. Chem. Lett. 20, 6052–6055.

Rani, J., Kumar, S., Saini, M., Mundlia, J., Verma, P.K., 2016. Biological potential of pyrimidine derivatives in a new era. Res. Chem. Intermed. 42, 6777–6804.

Roe, D.R., Cheatham III, T.E., 2013. PTRAJ and CPPTRAJ: software for processing and analysis of molecular dynamics trajectory data. J. Chem. Theory Comput. 9, 3084–3095.

Sawant, R., Sarode, V., 2011. Synthesis, spectral characterization and analgesic activity of 2-methylthio-1, 4-dihydropyrimidines. Iran. J. Pharm. Res. IJPR 10, 733.

Seth, S.K., 2018. Structural characterization and Hirshfeld surface analysis of a CoII complex with imidazo [1, 2-a] pyridine. Acta Crystallogr. Sect. E Crystallogr. Commun. 74, 600–606.

Sheldrick, G.M., 2003. SHELXTL. Version 6.14. Structure Determination Software Suite. Bruker AXS, Madison (WI, USA).

Sheldrick, G.M., n.d. SHELXTL, v. 6.12, Structure Determination Software Suite,(2001) Bruker AXS. Madison, Wisconsin, USA

Siddique, S.A., Arshad, M., Naveed, S., Mehboob, M.Y., Adnan, M., Hussain, R., Ali, B., Siddique, M.B.A., Liu, X., 2021. Efficient tuning of zinc phthalocyanine-based dyes for dye-sensitized solar cells: a detailed DFT study. RSC Adv. 11, 27570–27582.

Silva, G.C.O., Correa, J.R., Rodrigues, M.O., Alvim, H.G.O., Guido, B.C., Gatto, C.C., Wanderley, K.A., Fioramonte, M., Gozzo, F.C., de Souza, R.O.M.A., 2015. The Biginelli reaction under batch and continuous flow conditions: catalysis, mechanism and antitumoral activity. RSC Adv. 5, 48506–48515.

Terracciano, S., Lauro, G., Strocchia, M., Fischer, K., Werz, O., Riccio, R., Bruno, I., Bifulco, G., 2015. Structural insights for the optimization of dihydropyrimidin-2 (1 H)-one based mPGES-1 inhibitors. ACS Med. Chem. Lett. 6, 187–191.

Trott, O., Olson, A.J., 2010. AutoDock Vina: improving the speed and accuracy of docking with a new scoring function, efficient optimization, and multithreading. J. Comput. Chem. 31, 455–461.

Turner, M.J., Thomas, S.P., Shi, M.W., Jayatilaka, D., Spackman, M. A., 2015. Energy frameworks: insights into interaction anisotropy and the mechanical properties of molecular crystals. Chem. Commun. 51, 3735–3738.

Yadlapalli, R.K., Chourasia, O.P., Vemuri, K., Sritharan, M., Perali, R.S., 2012. Synthesis and in vitro anticancer and antitubercular activity of diarylpyrazole ligated dihydropyrimidines possessing lipophilic carbamoyl group. Bioorg. Med. Chem. Lett. 22, 2708–2711.

Zhu, X., Zhao, G., Zhou, X., Xu, X., Xia, G., Zheng, Z., Wang, L., Yang, X., Li, S., 2010. 2, 4-Diaryl-4, 6, 7, 8-tetrahydroquinazolin-5 (1H)-one derivatives as anti-HBV agents targeting at capsid assembly. Bioorg. Med. Chem. Lett. 20, 299–301.